



OPEN

# Electrochemical deposition of bimetallic sulfides on novel BDD electrode for bifunctional alkaline seawater electrolysis

Mingxu Li<sup>1,2</sup>, Genjie Chu<sup>1,2</sup>, Jiyun Gao<sup>1,3</sup>, Xiaolei Ye<sup>1,2</sup>✉, Ming Hou<sup>1,2</sup>, Shenghui Guo<sup>1,2</sup>, Yunchuan Li<sup>1,2</sup>, Ziqi Zhou<sup>1,2</sup>, Li Yang<sup>1,2</sup>✉ & Pascal Briois<sup>4</sup>

Seawater electrolysis is an ideal technology for obtaining clean energy—green hydrogen. Developing efficient bifunctional catalysts is crucial for hydrogen production through direct seawater electrolysis. Currently, metal substrates loaded with active catalysts are widely employed as electrodes for seawater electrolysis. However, the challenge of metal corrosion cannot be ignored. In this work, the boron-doped diamond (BDD) with excellent corrosion resistance was explored as a substrate for loading active catalysts in seawater electrolysis. A step-by-step electrodeposition method was used to fabricate the FeCoS/Ni/BDD electrode, effectively addressing the poor adhesion of the FeCoS active layer to the BDD substrate. The resulting electrode demonstrated interesting bifunctional catalytic performance, achieving oxygen evolution reaction (OER) and hydrogen evolution reaction (HER) overpotentials of 425 mV and 360 mV, respectively, in alkaline simulated seawater (1 M KOH and 3.5 wt% NaCl) at a current density of 100 mA cm<sup>-2</sup>. Furthermore, by increasing the KOH concentration in the alkaline simulated seawater to 3 M, the OER and HER overpotentials of the electrode significantly decreased to 383 and 300 mV, respectively. This work offers a novel approach for utilizing BDD substrates in the design of corrosion-resistant electrodes for alkaline seawater electrolysis.

**Keywords** Boron-doped diamond, Seawater electrolysis, Bifunctional catalyst, Bimetallic sulfide, Corrosion resistance

The depletion in fossil energy and the rise in environmental pollution have made the development of renewable clean energy an increasingly urgent concern<sup>1,2</sup>. Among various renewable energy sources, hydrogen energy stands out as an ideal alternative to traditional fossil fuels due to its high energy density, excellent calorific value, and environmentally friendly nature<sup>3–5</sup>. Currently, hydrogen energy is primarily produced from fossil fuels, industrial by-products, methanol reforming, and water electrolysis<sup>6,7</sup>. Among these methods, hydrogen production through seawater electrolysis is particularly attractive due to its clean process and zero carbon emissions<sup>8–10</sup>. However, the widespread adoption of hydrogen production via water electrolysis is hindered by significant overpotential energy losses<sup>11–13</sup>. Hydrogen production through water electrolysis, where catalysts play a key role in economic viability and environmental sustainability, is demonstrated. Platinum electrodes are widely used in three-electrode devices for electrochemical analysis because of their excellent electrochemical inertness, electrical conductivity, and mechanical stability<sup>14</sup>. However, these electrodes still encounter problems related to high potential and cost. The corrosion resistance of transition metal sulfides is significantly enhanced in acidic and alkaline environments<sup>15–18</sup>. Hui Su et al. effectively modulated the electronic structure of sulfides through the introduction of defects, vacancies, and morphology modulation. This efficient modulation resulted in a reduction in the oxygen evolution reaction (OER) energy barriers and an enhancement in the electrochemical properties<sup>17,19,20</sup>. Wei Liu et al. treated nickel foam (NF) with Al-doped Ni<sub>3</sub>S<sub>2</sub> to obtain Al-Ni<sub>3</sub>S<sub>2</sub>/NF composites. The test results indicated that the low overpotentials of hydrogen evolution reaction (HER) and OER were determined to be 86 and 223 mV, respectively, at a current density of 10 mA/cm<sup>2</sup> in a 1 M KOH solution<sup>21</sup>.

<sup>1</sup>Faculty of Metallurgical and Energy Engineering, Kunming University of Science and Technology, Kunming 650093, China. <sup>2</sup>State Key Laboratory of Complex Nonferrous Metal Resources Clean Utilization, Faculty of Metallurgical and Energy Engineering, Kunming University of Science and Technology, Kunming 650093, China. <sup>3</sup>School of Chemistry and Environment, Yunnan Minzu University, Kunming 650093, China. <sup>4</sup>FEMTO-ST Institute (UMR CNRS 6174), UBFC/UTBM. Site de Montbéliard, 90010 Belfort, France. ✉email: Stoneye2@163.com; yanglikmust@163.com

NF metal substrates have significant advantages such as high electrical conductivity, large specific surface area, high mechanical strength, and easy processing. However, under industrial-grade electrolyzed water conditions, NF foam metal substrates encounter several corrosion resistance issues. Therefore, under extreme conditions, substrates with better corrosion resistance and a wider range of applications need to be developed.

The corrosion resistance of BDD electrodes in complex environments is mainly due to their unique electrochemical properties and potential for application in specific environments<sup>16,22</sup>. BDD electrodes show excellent corrosion resistance and catalytic activity in wastewater treatment, which enable them to effectively treat difficult-to-degrade industrial wastewater and enhance its biochemistry<sup>23,24</sup>. In certain gas detection applications, BDD can be used as a sensor in corrosive gas environments, such as chlorine and sulfur dioxide<sup>22,25–27</sup>. Electrodes made of BDD are commonly used to detect heavy metal ions such as lead and mercury in water bodies<sup>22,28</sup>. Meanwhile, the exploration of alternative materials and methods for seawater electrolysis includes the design of efficient and stable catalysts, system optimization, electrolyzer innovations, and emerging materials and technologies for electrocatalytic seawater decomposition<sup>29,30</sup>. The high corrosion resistance of the BDD electrode allows it to avoid various energy consumption problems caused by corrosion issues of the metal substrate compared with the traditional metal electrode. Therefore, in this study, we attach cobalt–iron sulfide to the BDD electrode to address certain related problems. Research on current hotspots such as seawater electrolysis is lacking. Therefore, expanding additional electrochemical applications of BDD electrodes and studying the feasibility and practicality of their implementation are important.

In this study, we propose a two-step process for fabricating CoFeS/Ni/BDD electrodes. This process involves electroplating a nickel layer onto BDD electrodes and subsequently depositing cobalt–iron sulfides electrochemically. The structure and morphology of the crystals were characterized by XRD and SEM, and the electrochemical properties of the electrodes were tested by means of linear scanning voltammetry (LSV), cyclic voltammetry (CV), and alternating current impedance (EIS). Increasing the concentration of KOH reduces the overpotential for hydrogen and OERs. This approach offers a new solution to lowering the evolution potentials.

## Experimental Materials

Boron-doped diamond (BDD, 10 mm × 10 mm, single side) was purchased from New Peak Technology Co. Nickel metal plate (Ni, 25 mm × 25 mm × 1.5 mm) was sourced from Seiko Metal Materials Co. The chemical reagents used in the experiments, including ammonium chloride (NH<sub>4</sub>Cl), nickel chloride (NiCl<sub>2</sub>·6H<sub>2</sub>O), ferric chloride hexahydrate (FeCl<sub>3</sub>·6H<sub>2</sub>O), ammonia (NH<sub>3</sub>), potassium hydroxide (KOH), sodium chloride (NaCl), thiourea (CH<sub>4</sub>N<sub>2</sub>S), potassium chloride (KCl), anhydrous ethanol (C<sub>2</sub>H<sub>5</sub>OH) were purchased from Tianjin Zhiyuan Chemical Reagent Co.

### Preparation of CoFeS/Ni/BDD electrode

As illustrated in Fig. 1, CoFeS/Ni/BDD electrode were synthesized using BDD as substrate. Firstly, a Ni layer was deposited on the surface of BDD by electroplating to improve the adhesion of cobalt–iron sulfide on the surface of BDD. Subsequently, cobalt–iron sulfide was deposited on Ni/BDD to obtain CoFeS/Ni/BDD electrode. The detailed preparation process can be found in the supplementary.

Meanwhile, the concentration ratios of CoCl<sub>2</sub> to FeCl<sub>3</sub> (Co/Fe is used instead of CoCl<sub>2</sub> to FeCl<sub>3</sub> for all subsequent ratios) were set to 1, 1.5, 2, and 3 (7.5 mM: 7.5 mM, 11.25 mM: 7.5 mM, 15 mM: 7.5 mM, 22.5 mM: 7.5 mM). The number of electrodeposition cycles is directly related to the amount of cobalt, iron, and sulfur deposited onto the Ni electrode. This number remains a key factor influencing the electrocatalytic performance of the electrode. For this purpose, four CoFeS/Ni/BDD electrodes were prepared by CV with a set scan rate of 5 mV s<sup>-1</sup> and a scan range of -0.6 V to 0.2 V. Each electrode underwent a different number of electrodeposition

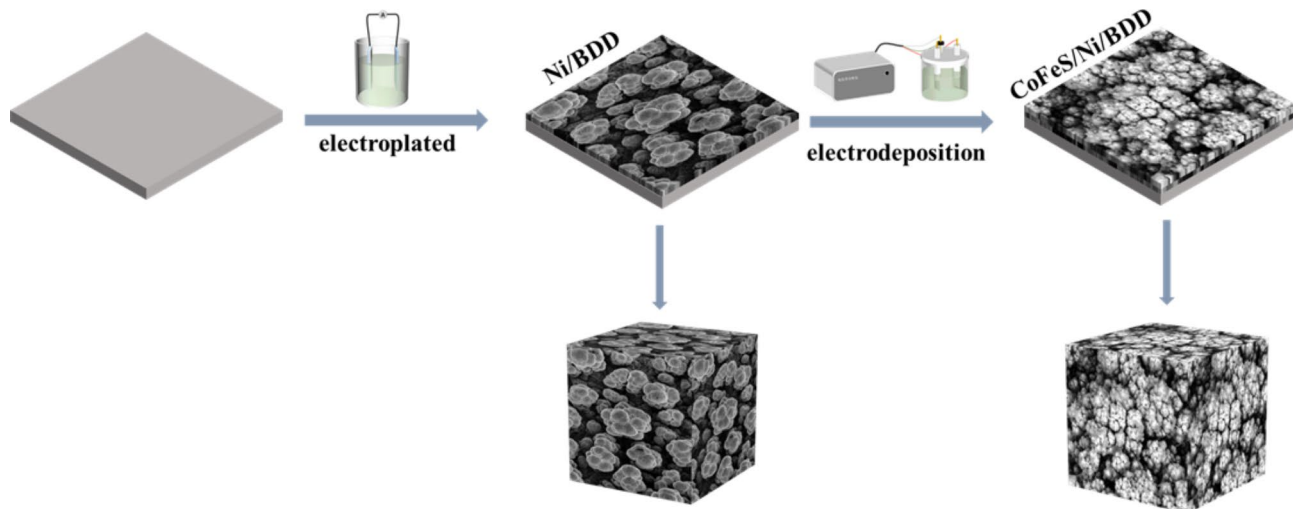


**Fig. 1.** Syntheses of CoFeS/Ni/BDD electrode.

cycles (5–20 turns). Ultimately, the appropriate cobalt–iron concentration and number of electrodeposition turns were selected based on the catalytic performance of these electrodes in a 1 M KOH solution.

## Material characterization

The BDD electrode-related information was characterized on a Bruker D8-Advance X-ray diffractometer (Cu K $\alpha$ ,  $\lambda = 1.5406 \text{ \AA}$ ) with a scanning speed of 3° per minute and a scanning range of 10°–100°. Using the JSM-7500 F model Scanning Electron Microscope (SEM) from Japan's JEOL company to observe the surface morphology of the sample, and with the addition of accessories such as an Energy Dispersive Spectrometer (EDS), the chemical composition of the sample can be analyzed. Using the Thermo Fisher Scientific model X-ray Photoelectron Spectroscopy (XPS) produced in the United States for the analysis of surface elemental valence state changes. Using a Japanese-made JEOL JEM-2100 transmission electron microscope (TEM) to analyze the crystal structure and chemical composition of the sample. Using the Raman spectrometer (SENTERRA II) produced by the German company Bruker Optics, the presence of M–S bonds in the sample can be accurately detected. Using the German Dataphysics Contact Angle Meter OCA25 to measure the wettability of materials.

## Electrochemical measurements

Electrochemical tests were conducted using a three-electrode system on the Shanghai Chenhua CHI760e electrochemical workstation. These tests included cyclic voltammetry (CV), linear sweep voltammetry (LSV), and electrochemical impedance spectroscopy (EIS). For seawater electrolysis experiments, the three-electrode system featured a boron-doped diamond (BDD) or BDD-based composite electrode as the working electrode. The working electrode had a total area of  $10 \times 10 \text{ mm}^2$ , with an immersed area of  $10 \times 5 \text{ mm}^2$ . A Hg/HgO or Ag/AgCl electrode was used as the reference electrode, while a carbon rod served as the counter electrode.

## Results and discussion

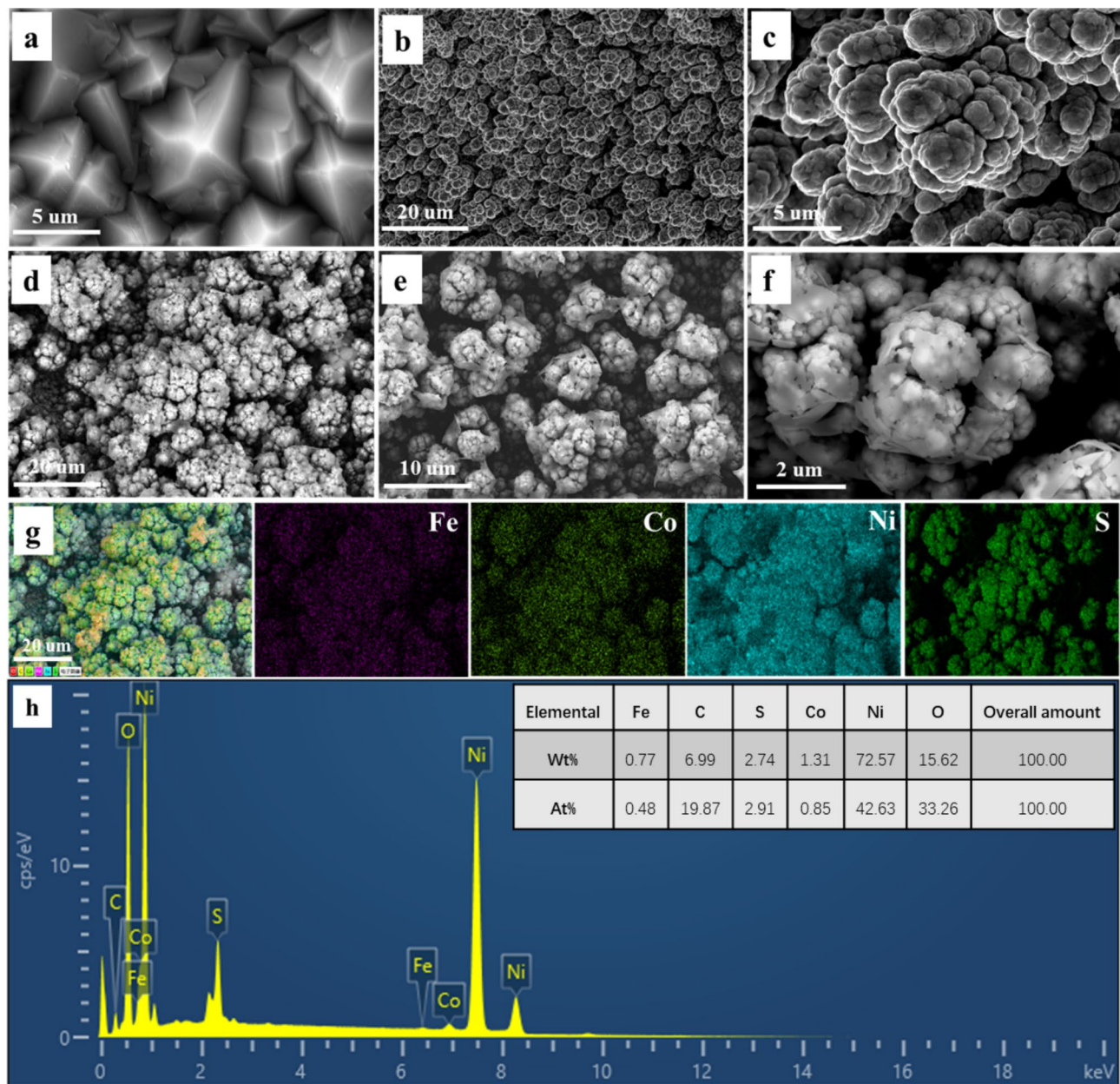
### Synthesis and structural characterization

Figure 2 illustrates the surface morphology and chemical composition of the electrode samples at various stages of the preparation process. High-quality BDD surfaces exhibit smooth polycrystalline pyramidal structures, with tightly textured BDD films formed by their intricate arrangement (Fig. 2a). SEM images of the Ni/BDD samples at different magnifications (Figs. 2b,c) reveal the agglomeration of cauliflower-like particles and a uniformly distributed columnar structure. The well-defined grooves between each column effectively increase the specific surface area, allowing for greater exposure of active sites. The morphology of the CoFeS/Ni/BDD electrode after electrodeposition was shown in Figs. 2d–f. A substantial amount of lamellar material is dispersed over the columnar structures and embedded within the cauliflower-like particles. This morphological transformation reflects the attachment of cobalt–iron sulfide to the electrode surface. The elemental composition of the CoFeS/Ni/BDD electrode surface was further analyzed and is presented in Figs. 2g, h. The results indicate that the nickel particles were completely encapsulated by the uniformly distributed elements. The analysis of elemental content in Fig. 2h also shows that Co, Fe, and S were deposited onto the surface of Ni/BDD to form a CoFeS/Ni/BDD electrode. Figure S1a shows the BDD electrode and CoFeS/Ni/BDD electrode, respectively. The characteristic diffraction peaks of diamond appeared in the vicinity of  $2\theta = 43.94^\circ, 75.22^\circ$  for the BDD electrode, which corresponded to the (111) and (220) crystal planes of the face-centered cubic diamond, respectively, and the intensity of diffraction peaks was largest for (111), which indicated that the BDD electrode was a diamond structure with a predominantly (111) crystal phase<sup>31</sup>. Three Ni diffraction peaks (PDF 04-0850) are observed at  $44.51^\circ, 51.84^\circ$ , and  $76.37^\circ$ , as demonstrated by the XRD spectra of the heat-treated CoFeS/Ni/BDD electrodes. The associated diffraction peaks of Ni–Co–S correspond to the standard card (JCPDS43-1477), which are observed simultaneously<sup>32</sup>. However, no obvious peaks of cobalt sulfide are observed, which can be attributed to the small amount deposited during electrodeposition of CoFeS<sup>33,34</sup>. In addition, a large number of  $\text{Ni}_3\text{S}_2$  diffraction peaks (PDF 44-1418) are detected. None of the observed information regarding iron sulfide is available. Thus, the electrodeposited iron sulfide was assumed to be amorphous. This assumption is consistent with the results of the previous tests.

In order to deeply investigate the microstructural properties of CoFeS/Ni/BDD composites, we employed transmission electron microscopy (TEM) technique for detailed analysis. The high resolution TEM images allowed the different grain orientations to be clearly observed as shown in Figs. S1b,c. Specifically, the (200) crystallographic orientation of  $\text{Ni}_3\text{S}_2$  grains is identified, the (311) crystallographic orientation of Ni–Co–S grains is observed, and the (111) crystallographic orientation of Ni grains is also determined. Further analysis showed that the crystal spacing of these facets are 0.204 nm, 0.283 nm, and 0.204 nm, respectively, which coincided with the results of the XRD spectra.

Different chemicals and their crystal structures can be identified using Raman spectroscopy, as shown in Fig. S2a. The Raman spectrum of the Fe–S system exhibits an asymmetric stretching vibration of the Fe–S bond at  $208 \text{ cm}^{-1}$ , while a symmetric Fe–S stretching vibration is revealed at  $287 \text{ cm}^{-1}$ . The broadening of the peak located at  $208 \text{ cm}^{-1}$  indicates significant disorder on the local bond length scale, as well as a decrease in the strength of interionic bonding due to lattice expansion<sup>35,36</sup>. In the Raman spectrum of the Co–S system, the characteristic peaks located at  $470 \text{ cm}^{-1}$  and  $663 \text{ cm}^{-1}$  represent the asymmetric stretching vibrations of the Co–S bond, and these peaks are distinctive markers of vibrational modes specific to the material<sup>37</sup>.

In order to evaluate the hydrophilicity of the samples, a contact angle test was carried out. From Fig. S2b, it can be seen that the contact angle of CoFeS/Ni/BDD is  $20.2^\circ$ , which is obviously hydrophilic. A possible explanation for this phenomenon lies in the fact that CoFeS, as a metal sulfide, is rich in sulfur atoms on its surface, and these groups of atoms are able to form hydrogen bonds with water molecules, thus enhancing the hydrophilic properties of the electrode surface<sup>38</sup>. It is also possible that defective states in the material, such as



**Fig. 2.** (a) SEM images of the original BDD, (b,c) Ni/BDD SEM maps at different magnifications, (d–f) Scanning electron micrographs of CoFeS/Ni/BDD at different magnifications and their (g,h) EDS patterns and analysis of surface element content of CoFeS/Ni/BDD sample.

vacancies or interstices, may act as sites for water molecule adsorption, thereby increasing the hydrophilicity of the material<sup>39</sup>.

### Electrochemical properties

#### *Electrochemical properties of CoFeS/Ni/BDD electrode*

The electrode samples indicated in Fig. 3 were prepared by electrodeposition in electrolytes with different cobalt and iron concentrations. The HER and OER properties of the electrode samples were tested in a 1 M KOH solution to explore the optimal deposition parameters for cobalt and iron concentrations.

CoFeS/Ni/BDD electrode materials were prepared by Co/Fe deposition technology. The electrochemical activity of this electrode was evaluated for HER and OER using various concentrations of Co in a 1 M KOH solution, and the LSV curves are shown in Figs. 3a,b. The HER and OER overpotential line plots for a single CoFeS/Ni/BDD electrode at the current densities of 100 and 200 mA cm<sup>-2</sup> were shown in Fig. 3c. The results reveal that the HER and OER overpotentials of the CoFeS/Ni/BDD samples were minimized when the Co/Fe concentration ratio was 1.5. This indicates that the electrocatalytic performance of this group of samples is

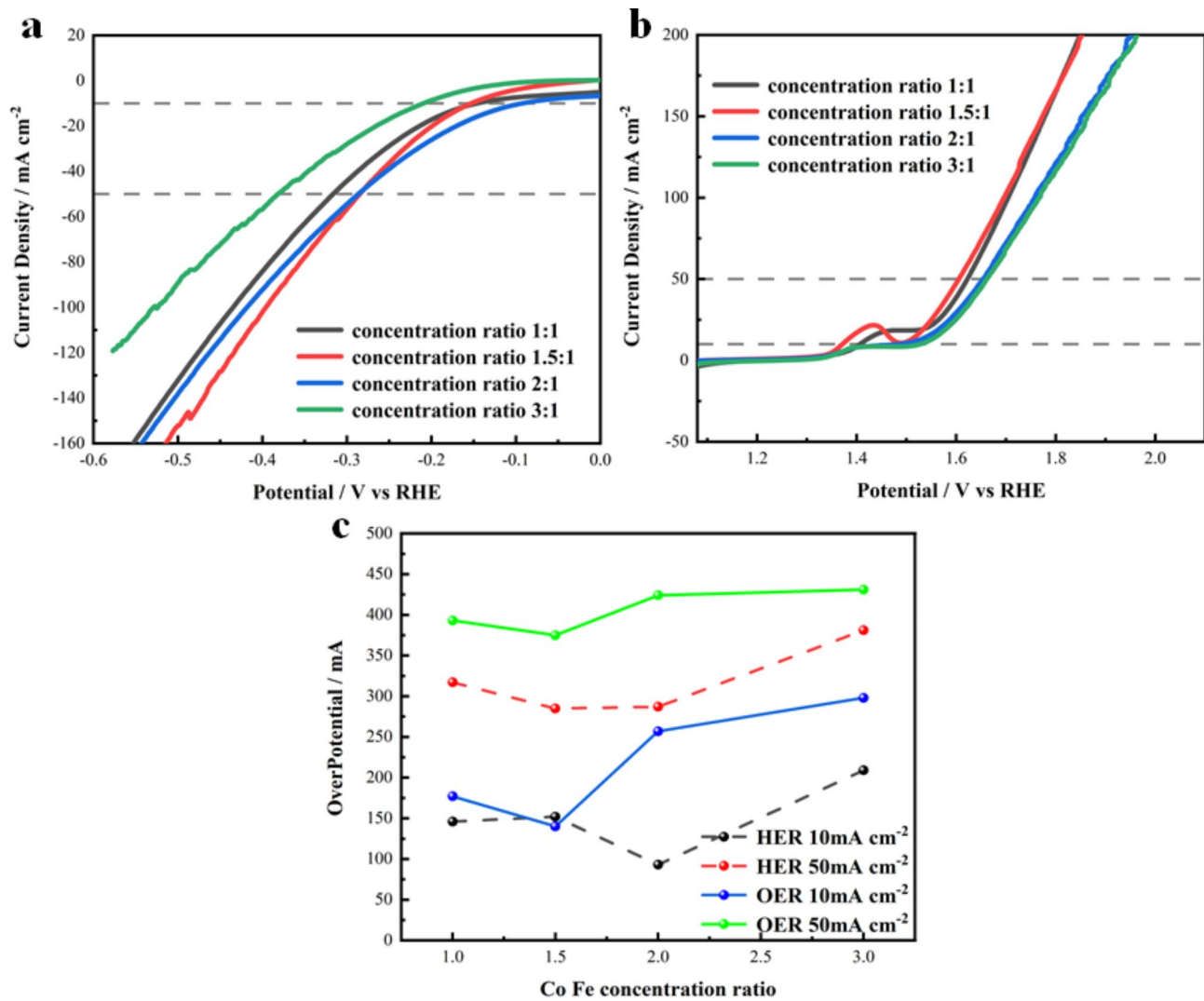


**Fig. 3.** CoFeS/Ni/BDD electrode prepared with different concentration ratios of cobalt and iron (a) HER performance, (b) OER performance and (c) overpotential line graph at current densities of  $10 \text{ mA cm}^{-2}$  and  $50 \text{ mA cm}^{-2}$ .

optimal. Unless otherwise specified, the CoFeS/Ni/BDD electrodes discussed later were prepared with a Co/Fe concentration ratio of 1.5.

The HER and OER performance of CoFeS/Ni/BDD electrodes prepared with different numbers of cycles was shown in Fig. 4. These results demonstrate that the number of electrodeposition cycles significantly affects the catalytic performance of the CoFeS/Ni/BDD electrodes. The electrodes exhibit the poorest performance when only 5 cycles were performed. However, the catalytic performance improves progressively as the number of cycles increases, reaching optimal performance at 15 cycles. Beyond this point, performance begins to decline, with the results for 20 cycles being similar to those for 10 cycles. The best HER and OER performance were achieved with 15 cycles, as shown in Figs. 4a,b. Figure 4c presents an analysis of the overpotential line graphs for the CoFeS/Ni/BDD electrode at current densities of  $100$  and  $200 \text{ mA cm}^{-2}$ .

In summary, the optimal process for the preparation of CoFeS/Ni/BDD electrodes by CV electrodeposition is determined as 15 cycles at a sweep rate of  $5 \text{ mV/s}$  in the range  $-0.6 \text{ V}$  to  $0.2 \text{ V}$ .

#### HER catalytic performance of CoFeS/Ni/BDD

The hydrogen evolution reaction (HER) performance of the CoFeS/Ni/BDD electrode was systematically evaluated. For comparison, pristine BDD, Ni/BDD, and CoFeS/Ni/BDD electrodes were tested in a  $1 \text{ M KOH}$  standard solution and an alkaline simulated seawater solution containing  $3.5\%$  NaCl and  $1 \text{ mol/L KOH}$ . Additionally, a control solution containing  $3.5\%$  NaCl and  $3 \text{ mol/L KOH}$  was included to examine the influence of KOH concentration on the electrocatalytic performance. To eliminate interference from dissolved oxygen, nitrogen was bubbled through the solution for  $20 \text{ min}$  prior to testing. Figure 5a displays the linear sweep voltammetry (LSV) curves of the pristine BDD, Ni/BDD, and CoFeS/Ni/BDD electrodes in a  $1 \text{ M KOH}$  standard solution, alongside the LSV curves of the CoFeS/Ni/BDD electrode in alkaline simulated seawater (CoFeS/Ni/BDD).

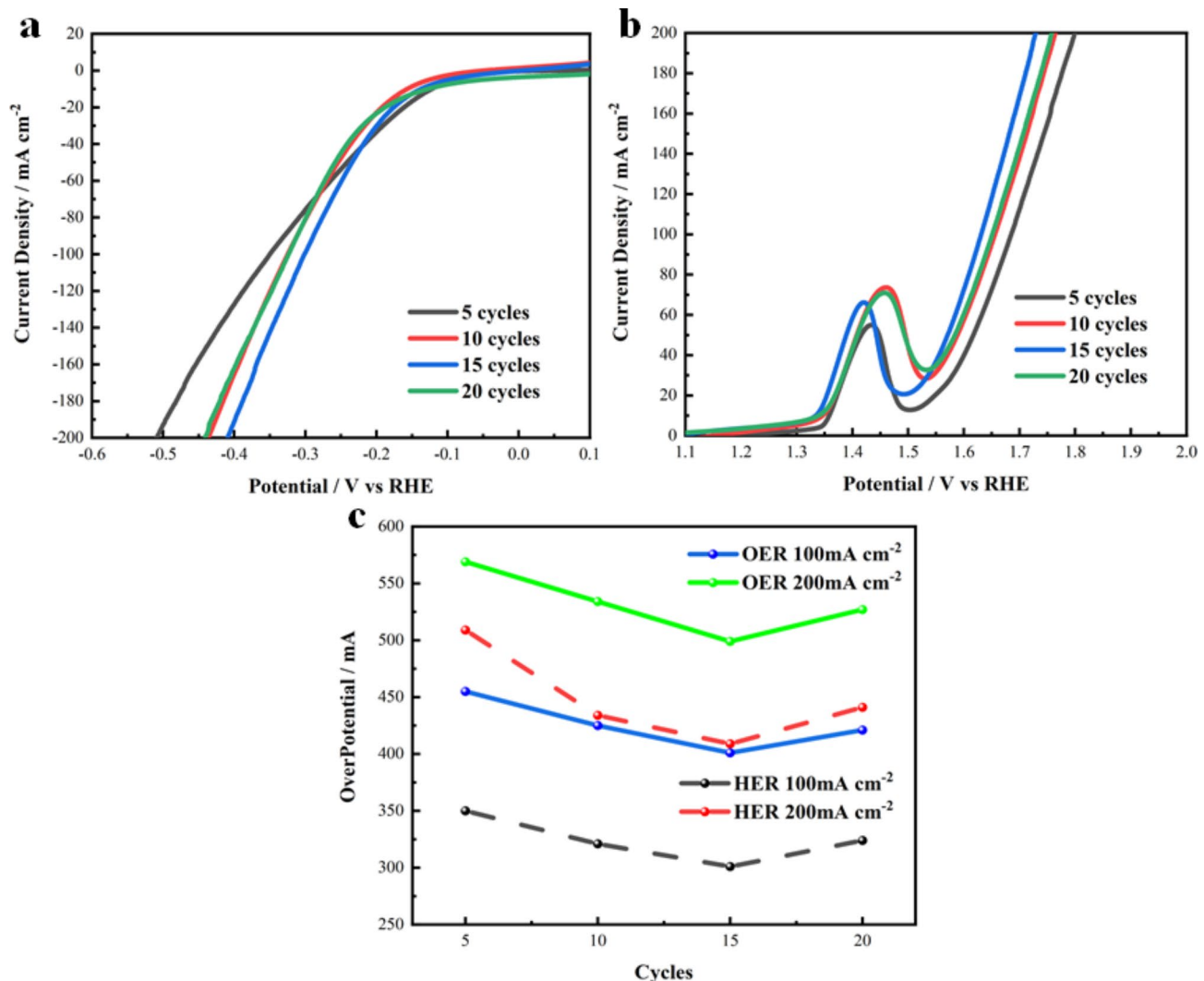


**Fig. 4.** (a) HER performance, (b) OER performance of the CoFeS/Ni/BDD electrode prepared with 5, 10, 15, and 20 electrodeposition cycles in the range of  $-0.6\sim 0.2$  V at a scan speed of 5 mV/s and (c) overpotential line graph at  $100 \text{ mA cm}^{-2}$  and  $200 \text{ mA cm}^{-2}$  current densities.

BDD-sea) at a sweep rate of 5 mV/s. In the 1 M KOH solution, the pristine BDD electrode demonstrates negligible HER activity, while the Ni/BDD electrode shows an overpotential of 345 mV. By contrast, the CoFeS/Ni/BDD electrode exhibits an overpotential of 325 mV, representing a 5.7% reduction. This improvement suggests that partial substitution of the Ni surface with NiCo and  $\text{Ni}_3\text{S}_2$  enhances HER activity, particularly at high current densities. In the alkaline simulated seawater solution, the overpotential of the CoFeS/Ni/BDD electrode increases to 360 mV due to a reduction in HER activity caused by NaCl. However, when the KOH concentration was increased to 3 M, the overpotential decreases to 300 mV, which is even lower than the value obtained in the 1 M KOH solution. This observation indicates that increasing the KOH concentration significantly enhances the catalytic performance. The HER Tafel slopes derived from the LSV curves (Fig. 5a) were shown in Fig. 5b. The CoFeS/Ni/BDD electrode exhibits a slope of 113.15 mV/dec in 1 M KOH, which increases to 130.81 mV/dec in alkaline simulated seawater. In comparison, the Ni/BDD electrode shows a higher slope of 165.92 mV/dec. Upon increasing the KOH concentration to 3 M, the Tafel slope of the CoFeS/Ni/BDD electrode decreases to 108.88 mV/dec. The comparison of Tafel slopes highlights the significant improvement in HER kinetics provided by the CoFeS/Ni/BDD electrode. This enhancement is attributed to the superior catalytic properties of novel materials such as nickel-cobalt alloys and nickel–iron sulfides, as well as the increased specific surface area resulting from the electrode's morphological features. Together, these factors contribute to the improved catalytic performance of the CoFeS/Ni/BDD electrode.

As shown in Fig. 5c, the charge transfer kinetics at the electrode-electrolyte interface were analyzed through electrochemical impedance spectroscopy (EIS) within the frequency range of 10 kHz to 0.01 kHz at a potential of -1.1 V vs. Hg/HgO. The BDD, Ni/BDD, and CoFeS/Ni/BDD electrodes were all tested in a 1 M KOH solution. The EIS data were plotted as Nyquist diagrams, where the charge transfer resistance ( $R_{\text{ct}}$ ) was determined by comparing the radii of the semicircles. The results reveal that the CoFeS/Ni/BDD electrode exhibits the smallest

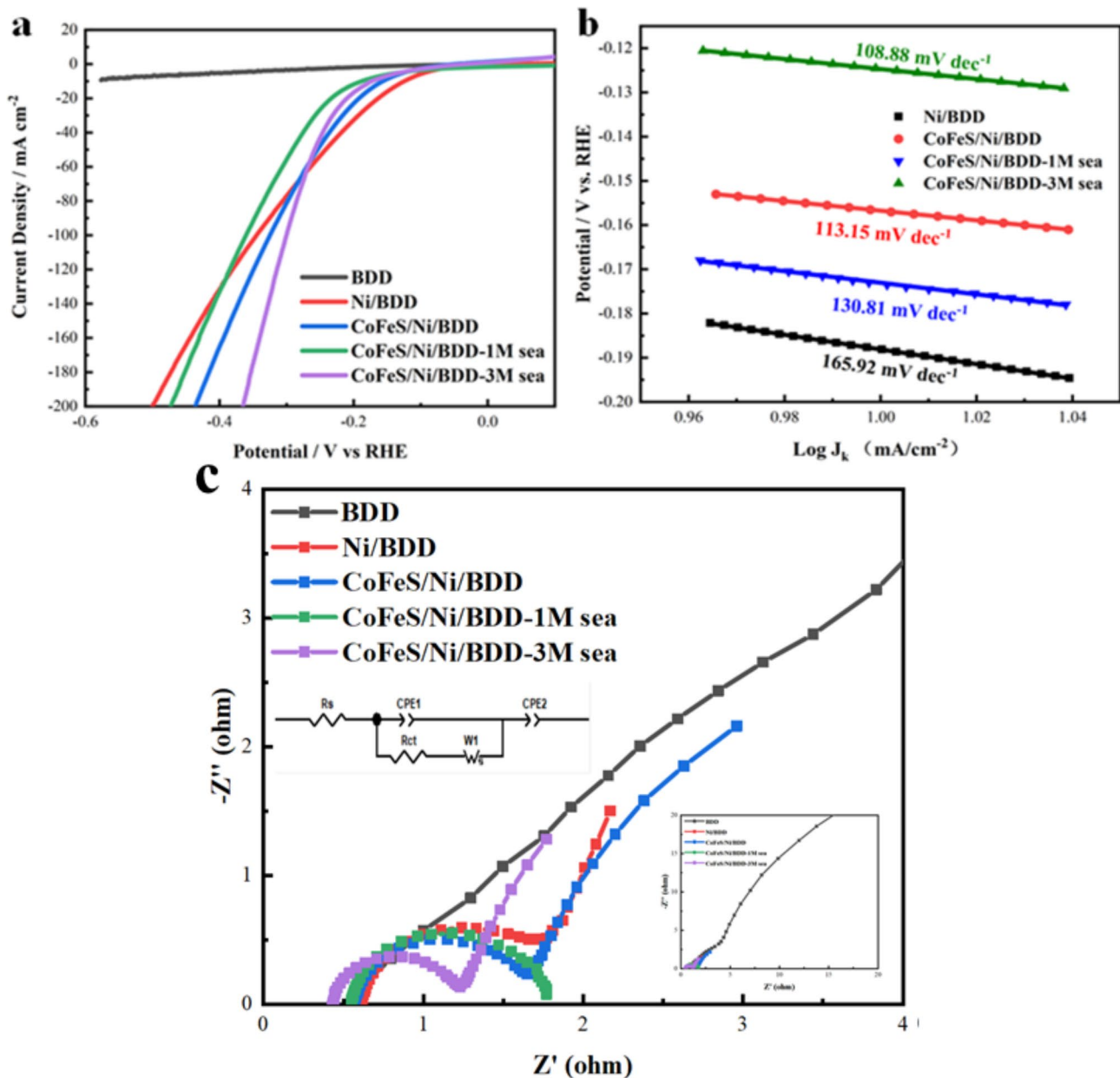


**Fig. 5.** (a) LSV inverse scan curve of each electrode of BDD, Ni/BDD, and CoFeS/Ni/BDD scanned in 1 M KOH solution or alkaline simulated seawater (1 M/3 M) at a scan rate of 5 mV/s. (b) Current Tafel curve when the density is 10  $\text{mA cm}^{-2}$ . (c) EIS curve relative to Hg/HgO when the potential is -1.1 V.

Nyquist radius, indicating the lowest  $\text{R}_{\text{ct}}$  and the fastest charge transfer during HER. Furthermore, when tested in a 3 M KOH simulated seawater solution, the Nyquist semicircle becomes even smaller, reflecting a further reduction in  $\text{R}_{\text{ct}}$  and an enhanced charge transfer rate. This improvement is attributed to the increased ionic concentration in the higher KOH solution, which reduces resistance and facilitates faster charge transfer at the interface.

#### OER catalytic properties of CoFeS/Ni/BDD

The oxygen evolution reaction (OER) catalytic activity of the electrodes at each preparation stage was evaluated in a 1 M KOH solution and alkaline simulated seawater. To ensure accurate results, the solution was oxygenated for approximately 20 mins before each test to achieve sufficient dissolved oxygen. Figure 6a presents the linear sweep voltammetry (LSV) curves of pristine BDD, Ni/BDD, and CoFeS/Ni/BDD electrodes in 1 M KOH, along with the CoFeS/Ni/BDD electrode in alkaline seawater (CoFeS/Ni/BDD-sea) at a sweep rate of 5 mV/s. The pristine BDD electrode demonstrates poor OER activity. In contrast, the Ni/BDD electrode, featuring a cauliflower-like Ni layer, reaches 1.685 V at a current density of 100  $\text{mA cm}^{-2}$ , corresponding to an overpotential of 455 mV. For the CoFeS/Ni/BDD electrode, the corresponding potentials are 1.631 V and 1.655 V in a 1 M KOH solution

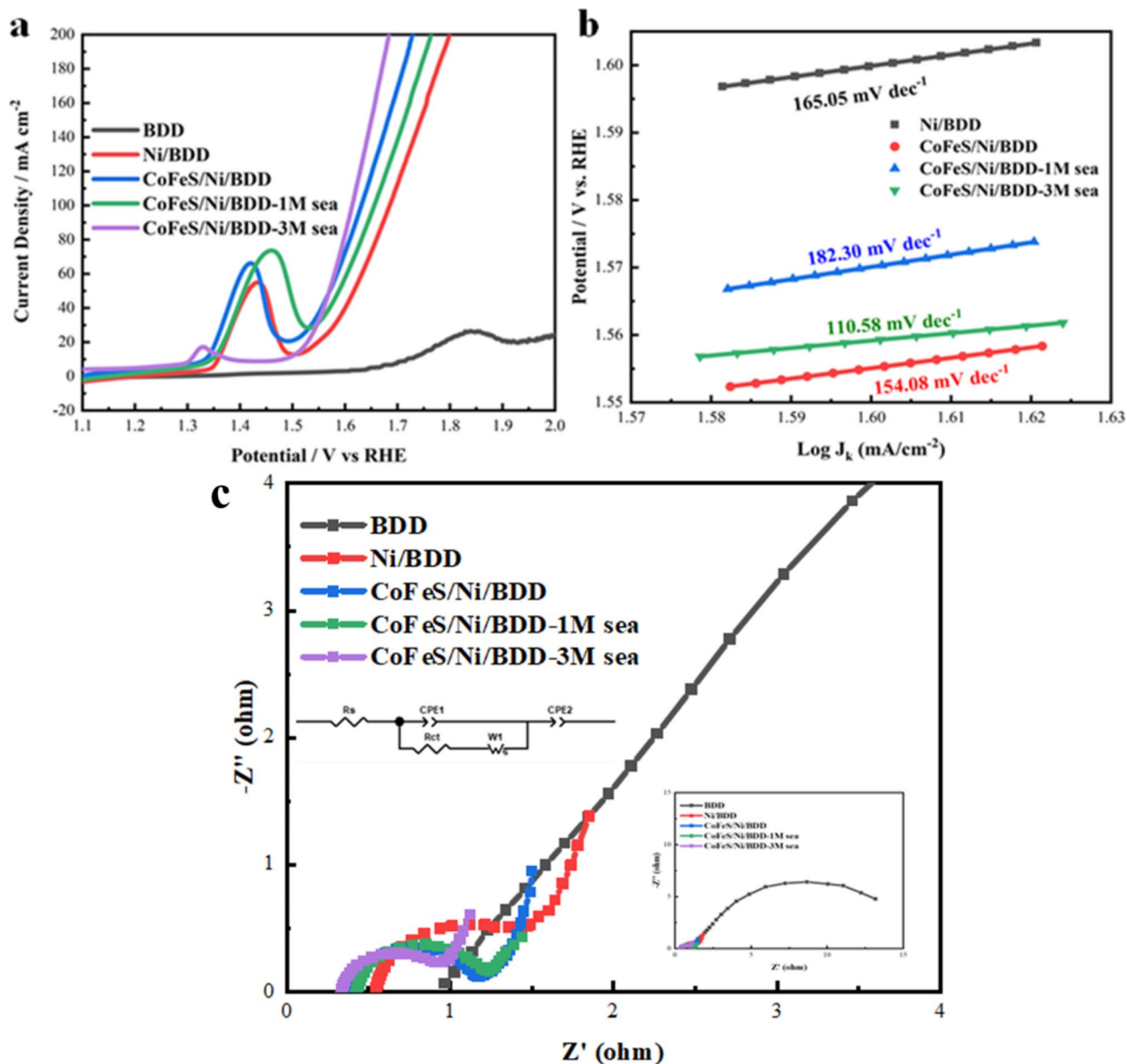


**Fig. 6.** (a) LSV inverse scan curve of each electrode of BDD, Ni/BDD, and CoFeS/Ni/BDD scanned in 1 M KOH solution or alkaline simulated seawater (1 M/3 M) at a scan rate of 5 mV/s. (b) Current Tafel curve when the density is 100  $\text{mA cm}^{-2}$ . (c) EIS curve relative to Hg/HgO when the potential is 0.6 V.

and alkaline simulated seawater, respectively, with overpotentials of 401 mV and 425 mV at 100  $\text{mA cm}^{-2}$ . These results highlight the significant enhancement in OER catalytic performance achieved with the CoFeS/Ni layer, particularly at high current densities. Additionally, increasing the KOH concentration reduces the oxygen evolution activation energy significantly, especially in seawater environments. This reduction helps suppress side reactions, further improving the efficiency of the OER process.

The Tafel curve for the OER was derived computationally from the LSV curve. As illustrated in Fig. 6b, the Tafel slope of the CoFeS/Ni/BDD electrode in a 1 M KOH standard solution was determined to be 154.08 mV/dec. This value increases to 182.30 mV/dec in alkaline simulated seawater. By contrast, the Tafel slope decreases to 110.58 mV/dec for the CoFeS/Ni/BDD electrode in simulated seawater containing 3 M KOH. For comparison, the Ni/BDD electrode without electrodeposition treatment exhibits a higher Tafel slope of 165.05 mV/dec. These findings indicate that the introduction of cobalt-iron sulfide significantly enhances the electrode's kinetic reactivity. This improvement is attributed to the high electrical conductivity of CoFeS and the partial oxidative conversion of surface catalysts into cobalt-iron oxides. However, the OER process is hindered by side reactions in the solution, leading to energy loss and reduced catalytic efficiency.

Electrochemical impedance spectroscopy (EIS) was used to study charge transfer during the OER (Fig. 6c). The frequency range was consistent with that used in HER experiments, and the potential was set to 0.6 V vs.

Hg/HgO. The results show that the CoFeS/Ni/BDD electrode in simulated seawater solution containing 3 M KOH exhibited the smallest Nyquist semicircles, the lowest charge transfer resistance ( $R_{ct}$ ), and the fastest charge transfer rates during the OER. The standard 1 M KOH solution performed slightly worse, echoing trends observed in the HER tests. These results suggest that the preparation of CoFeS and increasing the KOH concentration significantly enhance the efficiency of seawater electrolysis.

The electrodeposition process of the cobalt–iron sulfide layer was studied at different stages by cycling the electrodes at various scanning speeds (0.1 V to 0.2 V vs. Hg/HgO) in a 1 M KOH solution. The nickel layer on the electrode was also periodically scanned under identical conditions to examine changes in the electrochemically active surface area (ECSA) at different stages. Figures S3a-c show the cyclic voltammetry (CV) curves for the pristine BDD, Ni/BDD, and CoFeS/Ni/BDD electrodes. The relationship between the current density difference ( $\Delta J$ ) and the scanning speed (representing the electric double-layer capacitance,  $C_{dl}$ ) is depicted in Fig. S3d. The  $C_{dl}$  value for the CoFeS/Ni/BDD electrode was calculated to be  $3.399 \times 10^{-2}$  mF/cm<sup>2</sup>, which is approximately 21.93 times greater than that of the pristine BDD electrode ( $1.550 \times 10^{-3}$  mF/cm<sup>2</sup>) and 1.53 times higher than that of the Ni/BDD electrode ( $2.226 \times 10^{-2}$  mF/cm<sup>2</sup>).

In summary, the BDD substrate was electroplated with a nickel layer that formed cauliflower-like agglomerates, providing the surface with a columnar and well-defined structure. This modification effectively increased the specific surface area. Subsequently, cobalt–iron sulfide was electrodeposited on the nickel layer, further enhancing the surface area. As a result, the contact area between the electrolyte and the catalyst was significantly increased, leading to improved catalytic performance.

#### *Effect of different potassium hydroxide concentrations on the electrocatalytic performance of CoFeS/Ni/BDD of CoFeS/Ni/BDD*

Seawater electrolysis can sometimes result in side effects that are quite troublesome. These side reactions compete with the OER and significantly impact the efficiency of oxygen generation on the anode. Enhancing the priority and efficiency of OER on the anode while minimizing or eliminating competing side reactions has become a critical focus of current research.

The OER activity of CoFeS/Ni/BDD electrodes improves significantly with increasing KOH concentration during electrocatalysis, as shown in Fig. 7b. When the KOH concentration increases from 1 M to 4 M, the OER overpotential at a current density of 200 mA cm<sup>-2</sup> decreases from 404 mV to 396 mV. Importantly, when the concentration reaches 3 M, the overpotential (405 mV) is lower than the side-reaction potential (410 mV) in the alkaline seawater electrolyte, suggesting that higher KOH concentrations can suppress side reactions at elevated current densities. Similarly, the HER overpotential decreases with increasing salinity, as shown in Fig. 7a. At a current density of 200 mA cm<sup>-2</sup>, the overpotential values drop from 473 mV at 1 M KOH to 396 mV at 4 M KOH. This reduction in overpotential can be attributed to the increased ion supply in the electrolyte, which enhances collision frequency and promotes the reaction rate. Figure 7c presents the HER and OER

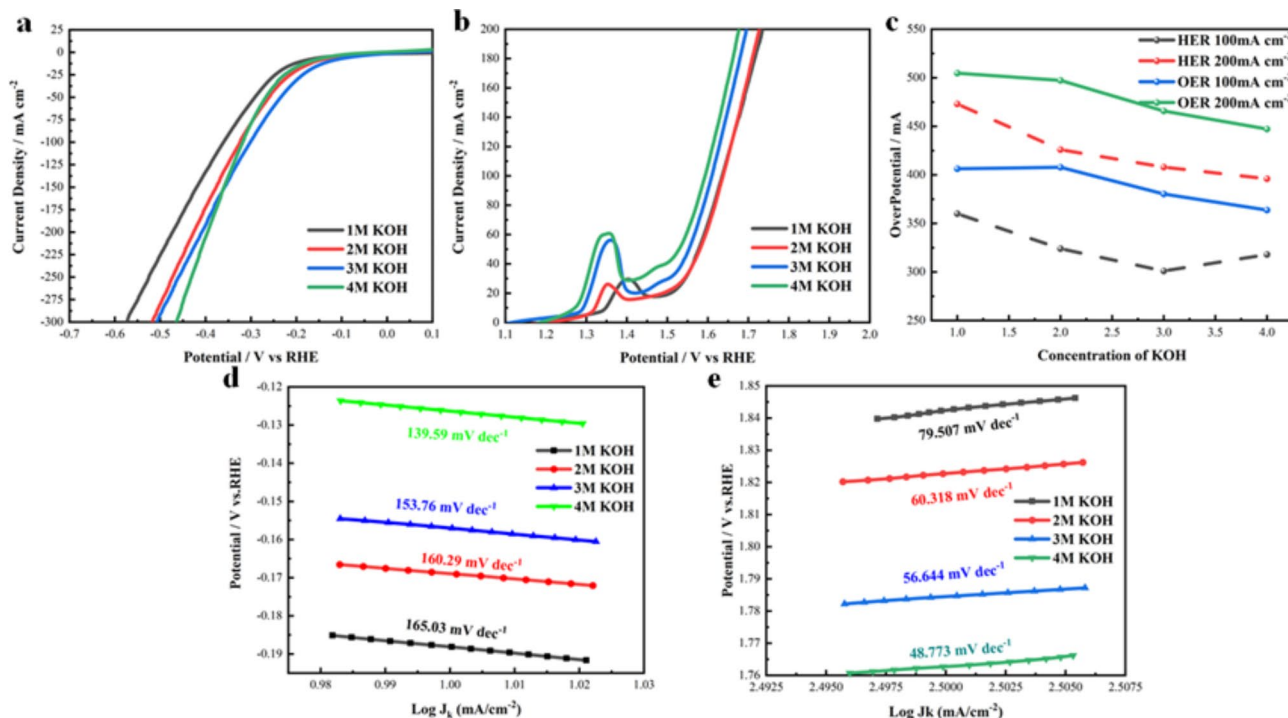


**Fig. 7.** (a) HER. (b) OER. (c) Overpotential line diagram of CoFeS/Ni/BDD electrode in 1 M, 2 M, 3 M, 4 M KOH solutions at 100 mA cm<sup>-2</sup> and 200 mA cm<sup>-2</sup> current density and (d) Tafel curve of HER at a current density of 10 mA cm<sup>-2</sup> and (e) Tafel curve of OER at a current density of 200 mA cm<sup>-2</sup>.

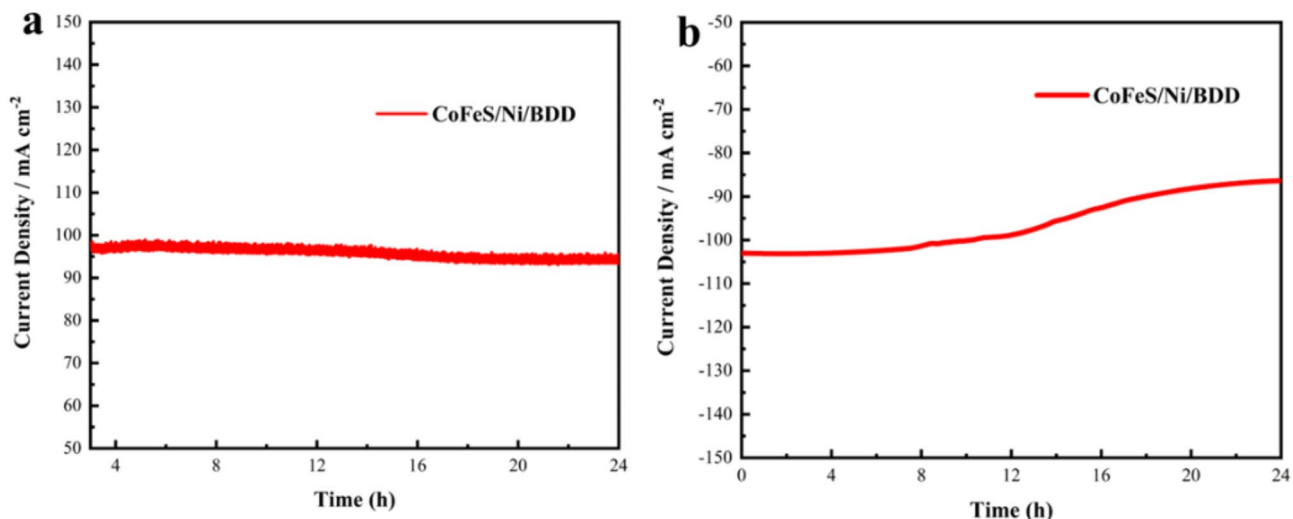


**Fig. 8.** (a,b) Chronoamperometry curves of CoFeS/Ni/BDD in real seawater containing 1 M KOH.

overpotential trends for CoFeS/Ni/BDD electrodes at current densities of 100 and 200  $\text{mA cm}^{-2}$  across different KOH concentrations. Both hydrogen and oxygen evolution improve as the KOH concentration increases, with the best catalytic performance observed in a 4 M KOH solution. The OER/HER Tafel curves, derived from the LSV curves (Figs. 7a,b), were shown in Figs. 7d,e. The Tafel slope values reveal a strong correlation with KOH concentration. For HER, the Tafel slope decreases from 165.03 mV/dec at 1 M KOH to 139.59 mV/dec at 4 M KOH, indicating enhanced reaction kinetics. Similarly, for OER, the Tafel slope drops from 79.51 mV/dec at 1 M KOH to 48.77 mV/dec at 4 M KOH, demonstrating significant improvement in catalytic performance. These results suggest that higher KOH concentrations not only enhance catalytic efficiency but also mitigate side reactions during seawater electrolysis. In specific scenarios, increasing the salt concentration in the electrolyte can further optimize the electrocatalytic effect.

In this work, we evaluated the stability of cobalt-iron sulfur electrodes for 24 h using the i-t method. In real seawater containing 1 M KOH, we investigated the HER and OER catalytic stability of the CoFeS/Ni/BDD electrode material using the timed-current method. The  $\text{Hg}/\text{HgO}$  potential of the CoFeS/Ni/BDD electrode was set to -1.38 V and the  $\text{Hg}/\text{HgO}$  potential was set to 0.68 V based on the potentials corresponding to a current density of 100  $\text{mA cm}^{-2}$ , and the stability tests were conducted for 24 h. After the 24 h stability test, the CoFeS/Ni/BDD electrodes were tested at the HER and OER levels. After the 24 h stability test, the current densities of the CoFeS/Ni/BDD electrodes at the OER and HER decayed to 92.62% and 84.31% of the original current densities, respectively (Figs. 8a,b). The slower decay rate at the OER than at the HER is due to the fact that the microstructure of the CoFeS/Ni/BDD electrodes may be more favorable to the OER, which reduces active substance shedding or other forms of performance during the reaction. substance shedding or other forms of performance degradation.

The surface morphology and microstructure of CoFeS/Ni/BDD electrodes after stability testing are demonstrated in Fig. S4. The dish-like agglomerated particles on the electrode surface were covered by hazy flocculent, but the overall structure of the catalyst remained unchanged, indicating that the catalyst on the BDD electrode was not dislodged, and the bonding between the two was strong (Figs. S4a-c) after 24 h. With the extension of time, flocculent buildup obscures the active sites and reduces the catalytic activity and environmental suitability of the electrode<sup>40</sup>.

CoFeS/Ni/BDD electrodes show very high stability in the oxygen precipitation reaction, which is mainly due to the highly stable BDD as the substrate can resist the occurrence of side reactions, and even if the catalyst on the surface is detached, it can still maintain a certain working capacity to ensure that the substrate electrode will not be broken.

## Conclusion

In this study, a cauliflower-like metallic nickel layer was initially plated onto the BDD surface. Subsequently, CoFeS/Ni/BDD electrodes with interesting bifunctional catalytic performance were fabricated by electrodepositing cobalt and iron sulfides onto the nickel layer. The optimal process parameters were identified as follows: a cobalt–iron concentration ratio of 1.5, a scanning speed of 5 mV/s, and a total of 15 electrodeposition cycles. The resulting electrode demonstrated low OER and HER overpotentials at a current density of 100  $\text{mA cm}^{-2}$  in alkaline simulated seawater. Furthermore, increasing the KOH concentration was found to significantly reduce the overpotentials and selectively enhance the OER, thereby improving the overall efficiency. This study not only broadens the application of BDD beyond its traditional use in the degradation of organic wastewater but also highlights its great potential in the field of seawater electrolysis. Moreover, it opens up new perspectives for the innovative utilization of BDD in advanced electrocatalytic applications.

## Data availability

All data in this thesis are publicly available, and anyone wishing to request data from this study should contact Dr. Yeh, Stoneye2@163.com.

Received: 11 September 2024; Accepted: 16 January 2025

Published online: 22 January 2025

## References

- Prajapati, M. & Shah, M. Geothermal-solar hybrid systems for hydrogen production: A systematic review. *Int. J. Hydrot. Energy.* **67**, 842–851 (2024).
- Dang, V. H. et al. Photocatalytic hydrogen production from seawater splitting: Current status, challenges, strategies and prospective applications. *Chem. Eng. J.* **484**, 149213 (2024).
- Du, J., Zhang, X., He, F. & Xie, Y. Modulation of the morphology, composition, and oxidation state of the spinel high-entropy oxides to boost their bifunctional catalytic activity for overall water splitting. *Electrochim. Acta.* **461**, 142599 (2023).
- Santra, S., Das, D., Das, N. S. & Nanda, K. An efficient on-board metal-free nanocatalyst for controlled room temperature hydrogen production electronic supplementary information (ESI) available. *Chem. Sci.* **8**, 2994–3001 (2017).
- Tarhan, C. & Çil, M. A study on hydrogen, the clean energy of the future: Hydrogen storage methods. *J. Energy Storage.* **40**, 102676 (2021).
- Jianlin, L., Zhonghao, L., Danxi, L. & Suliang, M. Overview of development status of green hydrogen production and application technology under targets of carbon peak and carbon neutrality. *Sci. Direct.* **6**, 25–33 (2021).
- Xu, S. & Yu, B. Current development and prospect of hydrogen energy technology in China. *J. Beijing Inst. Technol. (Soc. Sci. Ed.)* **23**, 1–12 (2021).
- Sun, H. et al. Electrochemical water splitting: Bridging the gaps between fundamental research and industrial applications. *Energy Environ. Mater.* **6**, 12441 (2023).
- Liu, Q. et al. F-doped self-supporting carbon electrode to improve carbon-water reaction assisted electrolysis of water for hydrogen production. *Fule* **375**, 132512 (2024).
- Li, W., Sun, Z., Ye, X. & He, Y. J. Ultra-thin PPS mesh-based PSF-ZrO<sub>2</sub> composite diaphragm for efficient electrolysis of water for hydrogen production. *Int. J. Hydrot. Energy.* **81**, 918–926 (2024).
- Zhang, W. et al. Research and perspectives on electrocatalytic water splitting and large current density oxygen evolution reaction. *Chin. J. Eng.* **45**, 1057–1070 (2023).
- Xie, W. F. & Shao, M. F. Alkaline water electrolysis for efficient hydrogen production. *J. Electrochem.* **28**, 4 (2022).
- Zhang, Y., Zhang, B. & Sun, J. Progress in hydrogen production by water electrolysis and its electrocatalysts. *Water Res.* **35**, 19 (2022).
- Wei, R., Fang, M., Dong, G. & Ho, J. C. Is platinum a suitable counter electrode material for electrochemical hydrogen evolution reaction? *Sci. Bull.* **62**, 971–973 (2017).
- Wang, S. et al. Arsenopyrite weathering in acidic water: Humic acid affection and arsenic transformation. *Water Res.* **194**, 116917 (2021).
- Kajana, T. et al. Potential transition and post-transition metal sulfides as efficient electrodes for energy storage applications. *RSC Adv.* **12**, 18041–18062 (2022).
- He, R., Huang, X. & Feng, L. Recent progress in transition-metal sulfide catalyst regulation for improved oxygen evolution reaction. *Energy Fuels.* **36**, 6675–6694 (2022).
- Noor, T., Yaqoob, L. & Iqbal, N. J. Recent advances in electrocatalysis of oxygen evolution reaction using noble-metal, transition-metal, and carbon-based materials. *ChemElectroChem* **8**, 447–483 (2021).
- Wang, M., Zhang, L., He, Y. & Zhu, H. Recent advances in transition-metal-sulfide-based bifunctional electrocatalysts for overall water splitting. *J. Mater. Chem. A.* **9**, 5320–5363 (2021).
- Jin, H. et al. Nanocatalyst design for long-term operation of proton/anion exchange membrane water electrolysis. *Adv. Energy Mater.* **11**, 2003188 (2021).
- He, W. et al. Al-doped nickel sulfide nanosheet arrays as highly efficient bifunctional electrocatalysts for overall water splitting. *Nanoscale* **12**, 24244–24250 (2020).
- Joshi, P., Riley, P., Goud, K. Y. & Mishra, R. K. Recent advances of boron-doped diamond electrochemical sensors toward environmental applications. *Curr. Opin. Electrochem.* **32**, 100920 (2022).
- Souza, A. B. et al. Occurrence and elimination of pharmaceutical residues in municipal wastewater effluent by electrochemical anodic oxidation. *J. Water Process. Eng.* **66**, 105899 (2024).
- Mackulak, T. et al. Boron doped diamond electrode—the elimination of psychoactive drugs and resistant bacteria from wastewater. *Vacuum* **171**, 108957 (2020).
- Zheng, Y., Zhang, Y. & Tong, Y. Research progress and application of boron-doped diamond film. *Highlights Sci. Eng. Technol.* **50**, 1138–1148 (2021).
- Zhou, Y. L., Tian, R. H. & Zhi, J. F. Amperometric biosensor based on tyrosinase immobilized on a boron-doped diamond electrode. *Biosens. Bioelectron.* **22**, 822–828 (2007).
- Zhou, Y. & Zhi, J. J. Development of an amperometric biosensor based on covalent immobilization of tyrosinase on a boron-doped diamond electrode. *Electrochim. Commun.* **8**, 1811–1816 (2006).
- Hao, Z., Yuxin, Z. & Jun, C. Direct electrochemical detection of ammonia in wastewater using boron-doped diamond (BDD) electrode. *Chin. J. Environ. Eng.* **15**, 4067–4076 (2021).
- Jin, H. et al. Emerging materials and technologies for electrocatalytic seawater splitting. *Sci. Adv.* **9**, 77559 (2023).
- He, W. et al. Materials design and system innovation for direct and indirect seawater electrolysis. *ACS Nano.* **17**, 22227–22239 (2023).
- Li, H. Y. et al. Research on the preparation of ozone by electrolysis of water using boron-doped diamond electrodes. *Appl. Chem. Ind.* **50**, 5 (2021).
- Bekar, L. G., Li, X. & Liu, W. Nickel cobalt sulfide core/shell structure on 3D graphene for supercapacitor application. *Sci. Rep.* **7**, 2105 (2017).
- Cheng, J. W. et al. Rational design of nickel cobalt sulfide/cobalt sulfide sheet-on-sheet structure for asymmetric supercapacitors. *Electrochim. Acta.* **283**, 1249–1252 (2018).
- Mohamed, M. S., Swaminathan, R., Mohan, V. & Liyakath, N. U. Sulfurization of cobalt oxide to cobalt sulfide: A positrode for the high-performance supercapacitor. *J. Ind. Eng. Chem.* **136**, 493–500 (2024).
- Matamoros Veloza, A. et al. A highly reactive precursor in the iron sulfide system. *Nat. Commun.* **9**, 3140–3156 (2018).
- Faber, M. S., Lukowski, M. A., Ding, Q., Kaiser, N. S. & Jin, S. Earth-abundant metal pyrites (FeS<sub>2</sub>, CoS<sub>2</sub>, NiS<sub>2</sub>, and their alloys) for highly efficient hydrogen evolution and polysulfide reduction electrocatalysis. *J. Phys. Chem. C.* **118**, 21347–21356 (2014).
- Wang, P. et al. S codoped carbon matrix-encapsulated CoFe/Co<sub>0.2</sub>Fe<sub>0.8</sub>S heterostructure as a highly efficient and durable bifunctional oxygen electrocatalyst for rechargeable zinc-air batteries. *J. Colloid Interface Sci.* **642**, 1–12 (2023).

38. Zhao, T., Zhong, D., Hao, G. & Zhao, Q. Vacancy engineering and hydrophilic construction of CoFe-MOF for boosting water splitting by *in situ* phytic acid treatment. *Appl. Surf. Sci.* **607**, 155079 (2023).
39. Muhammad, P. et al. Defect engineering in nanocatalysts: From design and synthesis to applications. *Adv. Funct. Mater.* **34**, 2314686 (2024).
40. Lee, S., Bai, L. & Hu, X. Deciphering iron-dependent activity in oxygen evolution catalyzed by nickel–iron layered double hydroxide. *Angew. Chem. Int. Ed.* **59**, 8072–8077 (2020).

## Acknowledgements

This research was supported by National Natural Science Foundation of China (52374389, 52364051) and Cai-yun Postdoctoral Program in Yunnan Province of China (CG24056E003A, CG24056E014A); The authors (Li Yang, Shenghui Guo) would like to acknowledge Xing Dian talent support program of Yunnan Province.

## Author contributions

Mingxu LI: methodology, formal analysis, investigation, data curation and writing - original draft. Genjie CHU: formal analysis and writing - review & editing. Jiyun GAO: formal analysis. Xiaolei YE: funding acquisition, supervision and writing - review & editing. Ming HOU: formal analysis. Shenghui GUO: funding acquisition, conceptualization. Yunchuan LI: formal analysis and software. Ziqi ZHOU: formal analysis. Li Yang: conceptualization, funding acquisition, supervision and writing - review & editing. Pascal BRIOIS: language review, formal analysis and visualization.

## Declarations

### Competing interests

The authors declare no competing interests.

### Additional information

**Supplementary Information** The online version contains supplementary material available at <https://doi.org/10.1038/s41598-025-87104-6>.

**Correspondence** and requests for materials should be addressed to X.Y. or L.Y.

**Reprints and permissions information** is available at [www.nature.com/reprints](http://www.nature.com/reprints).

**Publisher's note** Springer Nature remains neutral with regard to jurisdictional claims in published maps and institutional affiliations.

**Open Access** This article is licensed under a Creative Commons Attribution-NonCommercial-NoDerivatives 4.0 International License, which permits any non-commercial use, sharing, distribution and reproduction in any medium or format, as long as you give appropriate credit to the original author(s) and the source, provide a link to the Creative Commons licence, and indicate if you modified the licensed material. You do not have permission under this licence to share adapted material derived from this article or parts of it. The images or other third party material in this article are included in the article's Creative Commons licence, unless indicated otherwise in a credit line to the material. If material is not included in the article's Creative Commons licence and your intended use is not permitted by statutory regulation or exceeds the permitted use, you will need to obtain permission directly from the copyright holder. To view a copy of this licence, visit <http://creativecommons.org/licenses/by-nc-nd/4.0/>.

© The Author(s) 2025